Microcomputed Tomography and Microfinite Element Modeling for Evaluating Polymer Scaffolds Architecture and Their Mechanical Properties

Angel Alberich-Bayarri,[1] David Moratal,[2] Jorge L. Escobar Ivirico,[2,3] José C. Rodríguez Hernández,[2,3] Ana Vallés-Lluch,[2] Luis Martí-Bonmatí,[1] Jorge Más Estellés,[2] Joao F. Mano,[4] Manuel Monleón Pradas,[2,3,5] José L. Gómez Ribelles,[2,3,5] Manuel Salmerón-Sánchez[2,3,5]

[1] Radiology Department, Hospital Quirón, 46010 Valencia, Spain

[2] Center for Biomaterials and Tissue Engineering, Universidad Politécnica de Valencia, 46022 Valencia, Spain

[3] Networking Research Center on Bioengineering, Biomaterials and Nanomedicine (CIBER-BBN), Valencia, Spain

[4] 3B's Research Group-Biomaterials, Biodegradables and Biomimetics, Department of Polymer Engineering, University of Minho, 4710-057 Braga, Portugal

[5] Centro de Investigación Príncipe Felipe, 46013 Valencia, Spain

Received 14 September 2007; revised 15 October 2008; accepted 13 November 2008
Published online 7 May 2009 in Wiley InterScience (www.interscience.wiley.com). DOI: 10.1002/jbm.b.31389

Abstract: Detailed knowledge of the porous architecture of synthetic scaffolds for tissue engineering, their mechanical properties, and their interrelationship was obtained in a nondestructive manner. Image analysis of microcomputed tomography (μCT) sections of different scaffolds was done. The three-dimensional (3D) reconstruction of the scaffold allows one to quantify scaffold porosity, including pore size, pore distribution, and struts' thickness. The porous morphology and porosity as calculated from μCT by image analysis agrees with that obtained experimentally by scanning electron microscopy and physically measured porosity, respectively. Furthermore, the mechanical properties of the scaffold were evaluated by making use of finite element modeling (FEM) in which the compression stress–strain test is simulated on the 3D structure reconstructed from the μCT sections. Elastic modulus as calculated from FEM is in agreement with those obtained from the stress–strain experimental test. The method was applied on qualitatively different porous structures (interconnected channels and spheres) with different chemical compositions (that lead to different elastic modulus of the base material) suitable for tissue regeneration. The elastic properties of the constructs are explained on the basis of the FEM model that supports the main mechanical conclusion of the experimental results: the elastic modulus does not depend on the geometric characteristics of the pore (pore size, interconnection throat size) but only on the total porosity of the scaffold. © 2009 Wiley Periodicals, Inc. J Biomed Mater Res Part B: Appl Biomater 91B: 191–202, 2009

Keywords: scaffolds; mechanical properties; finite element analysis; tissue engineering

INTRODUCTION

Polymer scaffolds of well-defined architecture and mechanical properties are fundamental tools to be used in tissue engineering techniques. Synthetic scaffolds play the role of extracellular matrix that lead the organization of cells into a three-dimensional (3D) architecture and address the adequate mechanical stimuli, which direct the growth of the new tissue.[1–4]

Several intrinsic properties have been assigned to the ideal scaffold such as 3D interconnected pore network, biocompatibility, adequate surface properties to enhance cell adhesion and proliferation, and the adequate mechanical properties to match those of the surrounding tissue when implanted.[5–7] The mechanical properties of a synthetic scaffold depend on the physico-chemical properties of the material, its relative density, and the microstructural features.[8,9]

Correspondence to: M. Salmerón-Sánchez (e-mail: masalsan@fis.upv.es)
Contract grant sponsor: Programa de Apoyo a la Investigación y Desarrollo of the Universitat Politècnica de València; contract grant number: PAID-06-07/3104
Contract grant sponsor: Generalitat Valenciana; contract grant number: CTBPRB/2005/075
Contract grant sponsor: Spanish Ministry of Science (including the FEDER financial support); contract grant number: MAT2006-08120

There are different methods in the literature to produce 3D scaffolds such as phase separation,[5] emulsion freeze-drying,[10] gas foaming,[11] fiber templates,[12] porogen leaching,[13,14] and solid free fabrication (SFF)-rapid prototyping (RP), techniques that involve building 3D objects using layered manufacturing methods.[2,15] The design of scaffolds with controlled architecture continues being a central role in tissue engineering techniques.[16,17]

The desirable way to evaluate the scaffold 3D architecture after the fabrication process would be a nondestructive, noninvasive, and quantitative technique. Such goals can be obtained after suitable image analysis methodologies from microcomputed tomography images (μCT).[18] μCT is a technique to quantify the internal architecture of an object in three dimensions after image analysis. The specimen is irradiated with X-rays as it rotates through 180°. At each degree increment, a projection radiograph is taken. The series of projection radiographs are then reconstructed into 2D slices. Upon traversing through the specimen, the radiation is attenuated and it emerges with reduced intensity to be captured by the detector array. The attenuation is correlated with the material density and is typically represented as a gray scale conforming a 2D pixel map.

μCT allows resolutions of a few micrometers down to 100 nm if synchrotron facilities are used as the radiation source. μCT has been widely used to assess the trabecular bone structure and growth.[19–21] Only recently, it has been started to be used to investigate the 3D architecture of synthetic scaffolds,[22–25] as well as the tissue regeneration within the scaffold, mainly bone ingrowth.[26–30]

The use of finite element modeling (FEM) as an alternative tool to evaluate the mechanical properties of synthetic scaffolds is very convenient. The accuracy of the geometric modeling of the structure to be evaluated by FEM is very important and can be obtained in detail from μCT scans. The combined use of μCT reconstruction and FEM analysis as a tool for the design of synthetic scaffolds has been insufficiently investigated in the literature. The voxel simulation technique from digital images obtained from μCT was proposed by Hollister and coworkers[31] to study the bone remodeling phenomenon. Guldberg and coworkers[32] employed micro-CT images to create 3D high-resolution finite element models for estimating the local stress and strain distributions in bone. Jaecques et al.[33] performed μCT-based finite element modeling of native trabecular bone and bone scaffolds. In a more systematic way, Lacroix et al.[34] characterized macroporous calcium phosphate bone cement and porous phosphate glass first by μCT to investigate the porosity and then through the so-called μFEM (FE models obtained from μCT analysis) to evaluate the deformation observed by the cells attached to the material.

This work makes use of μCT and image analysis to investigate the 3D architecture of polymer scaffolds of different geometries (interconnected spherical pores, pores obtained from salt particles, and interconnected-perpendicular channels) and chemical composition (acrylates of different hydrophilicity and starch/poly(lactide) blends). Furthermore, the 3D model obtained is used to evaluate their mechanical properties by means of finite element modeling, μFEM. The geometric parameters are correlated with the mechanical results which, at the same time, are compared with experimental stress–strain measurements.

EXPERIMENTAL

Preparation of the Scaffolds

Constructs With Spherical Pores. Caprolactone 2-(methacryloyloxy)ethyl ester (CLMA) (Aldrich) and 2-hydroxyethyl acrylate (HEA) (Sigma-Aldrich, Madrid, Spain 96% pure) were employed without further purification. Benzoin (Aldrich, 98% pure) and ethylene glycol dimethacrylate (EGDMA) (Aldrich, 99% pure) were used as initiator and cross-linking agent, respectively. Acetone (Scharlau, Barcelona, Spain 99% pure) and ethanol (Aldrich, 99.5% pure) were used as solvents.

A detailed procedure regarding obtaining this particular pore architecture is explained elsewhere.[35] Poly(methyl methacrylate) (PMMA) microspheres of known size (90 ± 10 μm, Colacryl Durham, UK dp 300) were used as porogen introducing them between two plates (of a self-built device) whose distance can be controlled by adjusting the step of a coupled screw and heated at 180°C for 30 min to obtain the first template. This template shows the highest porosity attainable (that will yield the lowest porosity of the scaffold) with classical compaction values of 60–65% for random monosized spherical particles. To obtain scaffolds with controlled porosity, the thickness of the obtained disk was first measured; then, the disk was replaced in the mold and compressed at 180°C for half an hour. The degree of compression was quantified by measuring the thickness loss. A series of templates with varying degrees of compression were prepared. After cooling the template at room temperature, a monomer solution (in different weight proportions of both components 100/0, 70/30, 50/50, 30/70 CLMA/HEA) was introduced in the empty space between the PMMA spheres. The polymerization was carried out up to limiting conversion under a UV radiation source at room temperature. After polymerization took place, the PMMA matrix was removed by soxhlet extraction with acetone (Scharlau, synthesis grade) for 48 h. At this stage, the PMMA porogen template is completely removed. The porous sample is kept 24 h more in a soxhlet with ethanol to extract low-molecular weight substances. Samples were dried in vacuum until the weight was constant (differences below 1%) before characterization.

Constructs With a Cylindrical Orthogonal Pore Mesh. Ethyl acrylate (EA, Aldrich, 99% pure) was also used without further purification. EGDMA (1 wt %) and AIBN (0.1 wt %) were used as cross-linker agent and ther-

mal initiator, respectively. The monomeric solution polymerized undergoing bulk free radical polymerization when the temperature was raised up to 70°C for 24 h.

A detailed procedure regarding obtaining this particular pore architecture is explained elsewhere.[36] Briefly, a fixed number of polyamide 6.6 sheets of commercial textile fabrics (SAATI S.A., Barcelona, Spain) were used to build well-ordered structures to serve as porogenic templates. The nominal thread diameter of the employed fabrics was 150 μm.

The fabrics underwent a two-step process, which included compression and sintering of 25 stacked sheets. First, a simultaneous heating and compression stage was applied during 15 min in a hydraulic plate press. The temperature was kept constant during the compression step and 25°C below the onset of the melting point (T_{onset}) of polyamide 6 (T_{onset} = 245°C measured by differential scanning calorimetry in a heating scan to 10°C/min). Afterwards, a sintering process was carried out in an oven at a well-controlled temperature slightly higher than T_{onset} for 45 min, keeping a low-compression stress while sintering.

The filling of the available spaces within the templates was carried out by immersion of the produced templates into the monomeric solution. After polymerization, a material was formed in which the polyamide template was embedded inside. The polyamide 6 template was then dissolved by immersion at room temperature in nitric acid (Aldrich, 60% extra pure) for 4 days with several changes of the acid. After removing the template, the resulting porous materials were rinsed in boiling ethanol to remove any remaining chemicals. Finally, the scaffolds were dried in vacuo at 70°C to constant weight.

Constructs Based on Salt Particles. A 30/70 (wt %) blend of starch and poly(L-lactic acid) was also analyzed. Scaffolds were prepared by compression molding of the polymeric material compounded with salt particles, followed by salt leaching; porosity and pore size were controlled by changing the content of salt particle and particle size, respectively. The selected NaCl particle sizes were isolated by hand-sieved with stacked stainless steel sieves. The compression-molded discs of around 5 mm thickness and 80 mm diameter were prepared on a steel mold using a Moore hydraulic press (UK). The molded discs were sliced to ~5 × 5 × 5 mm^3 cuboids and put into water. The leaching was performed in beakers filled with deionized water at 37°C. The water was replaced in every 4 h until all the elimination of the salt.

Characterization of the Scaffolds

The volume fraction of pores in the scaffold, porosity, was determined gravimetrically by swelling the sample in water using a vacuum accessory. The porosity P is defined as follows:

$$P = \frac{V_{pore}}{V_{pore} + V_{polymer}}, \quad (1)$$

where V_{pore} is the part of the volume occupied by pores and $V_{polymer}$ is the volume occupied by the polymer. Let m_s^{sw} be the mass of the scaffold swollen in water and m_s^d the mass of the dry scaffold. Water sorbed in the scaffold is distributed between two phases as follows: water in pores and water sorbed in the polymer that forms the scaffold. Assuming that the equilibrium water content measured on dry basis (mass of water absorbed in equilibrium divided by the mass of dry polymer), w^*, of the material that constitutes the scaffold is the same as that of the bulk material of the same composition, the mass of water located in pores m_w^{pores} is as follows:

$$m_w^{pores} = m_s^{sw} - m_s^d - m_w^*, \quad (2)$$

where m_w^* is the mass of water absorbed in the polymer that forms the scaffold, that is,

$$m_w^* = m_s^d \cdot w^* \quad (3)$$

taking into account the density of water ρ_w, the amount of water located in pores gives their volume,

$$V_{pore} = \frac{m_s^{sw} - m_s^d(w^* + 1)}{\rho_w}. \quad (4)$$

The mass of water absorbed in equilibrium by the bulk polymer divided by the mass of the dry polymer, w^* was obtained from Ref. 35.

On the other hand, the volume of the scaffold occupied by the polymer can be obtained by measuring the density of the corresponding bulk material ρ_b.

$$V_{polymer} = \frac{m_s^d}{\rho_b}. \quad (5)$$

ρ_b was determined by weighing each one of the samples both in air and immersed in *n*-octane at 25°C. A Mettler Toledo (Barcelona, Spain) AE240 balance (sensitivity 0.01 mg) with density accessory Mettler Toledo ME3360 was employed. Porosity measurements were done at least in three different samples of each one of the compositions; porosity values were reproducible up to 3% and are shown in Table I.

Compression stress–strain measurements were performed on a Microtest machine (Madrid, Spain) with load cell of 15*N* at room temperature at a rate of 0.06 mm/s. Specimens for this test were cylinders, with a diameter of ~10 mm and 3 mm height. The guidelines in the ASTM D1621-00, standard Test Method for Compressive Properties of Rigid Cellular Solids were followed. The test was carried out until complete collapse of the microstructure. The experimental compressive modulus of the scaffold was not easy

TABLE I. Glass Transition Temperature (T_g, Onset) and Porosity for the Different Samples

Sample	T_g (°C)	Porosity (Experiment)	Porosity (μCT)	E_b (MPa)	E (MPa)	SCR	TEI
CLMA	−10	0.77	0.817	1	0.0380	11.600	0.570
CLMA70	−8	0.76	0.798	0.8	0.0360	5.594	0.742
CLMA50	−6	0.69	0.728	0.7	0.010	5.987	0.823
CLMA30	1	0.67	0.727	0.5	0.008	3.333	1.415
D150	−15	0.55	0.513	1	0.260	3.575	1.468

Results from experimental measurements and analysis of the μCT images are included. The two subsequent columns on the right show the experimental bulk modulus of the material (E_b), which constitutes the scaffold and the experimental modulus of the scaffold (E). Finally, after applying the topological analysis, values grading the erosion of the scaffolds are given (SCR and TEI).

to measure since the surface of the sample is not perfectly flat and the complete contact between the plate of the compression machine and the specimen lead to underestimate the initial range of strains (0–0.1). Thus, the compressive modulus was determined from the initial linear slope of the curve after full contact between plate and specimen was ensured.

Scanning electron microscopy (SEM) was performed in a JEOL JSM 5410 (Tokyo, Japan) in secondary mode. Transverse and longitudinal slices of the dry samples were sputtered coated with gold before observation at an accelerating voltage of 15 kV.

Microcomputed Tomography

The pore architecture of the scaffolds was also examined by microcomputational tomography, μ-CT, using a Sky-Scan1072 system (Kontich, Belgium). The specimens were mounted on a rotary stage and scanned under a 40 kV source for a complete rotation of 360°, to obtain a set of 2D slices.

Scaffold Characterization Using Image Analysis

All image processing was carried out using MATLAB R2007a (The Mathworks, Natick, MA). The μCT images were processed as a series of 150–160 slices of 1024 × 1024 pixels with a spatial resolution of 7.13 μm.

Before performing a structural and mechanical analysis to the μCT images, a preprocessing consisting of segmentation and binarization steps was performed to reduce computational burden.

Segmentation. A squared ROI of 400 × 400 pixels was selected in each slice by an automated algorithm to process a representative sample of the scaffold. Resultant grayscale images were stored in a 3D matrix representing a 3D reconstruction of the specified volume of interest (VOI) of the scaffold, considering isotropic voxels.

Binarization. Images were converted to its binarized version to discriminate structure voxels from empty voxels. The optimum threshold value applied during binarization was calculated for each slice using Otsu's method.[37] Binarized images were stored in a 3D binary matrix compounding a logical representation of the VOI.

Morphological Study. The morphological parameters calculated were as follows: Structure Thickness (St.Th), Pore size (St.Sp), Structure Index (St.I), Porosity (P), and Structure Volume (SV). These parameters will be defined below, as well as the way they were computed. Different measurements and algorithms were applied to the 3D binary reconstruction to perform the full analysis.

Porosity and Structure Volume. Porosity (P) was easily calculated by dividing the number of nonzero elements of the 3D reconstruction by the global number of elements of the VOI. This parameter is commonly expressed as a percentage. Partial volume voxels are not considered due to the high relationship between mean designed pore sizes (~90 μm) and the used spatial resolution (~7 μm). This parameter can be also expressed by its complementary, the structure volume (SV).

Structure Thickness. Measurement of St.Th was carried out in each plane of the 3D reconstruction. The developed algorithm used a 2D distance transform applied to each slice, where the skeleton or center line of the structure rods was calculated by a 2D skeletonization algorithm. Rod contours were also obtained by a 2D contour detection algorithm. Then, distance transform application to this last contour image provided the minimum distances of each pixel to a contour.[38] Results of distance transform application were then multiplied by the skeletonized slice. Therefore, the minimum distances of the skeleton pixels to the contour were obtained. This minimum distance corresponded to the half of the local rod thickness. Finally, a mean rod thickness was calculated for the whole scaffold by averaging with all the slices.

Structure Separation. Measurement of structure separation or mean pore size is assessed by a 3D algorithm. The method consisted of a structural voxel by voxel inspection. That is, in a given voxel corresponding to a pore (black

voxel), number of contiguous voxels on X direction are firstly counted, then the same is done for Y, and finally for Z. Then, if we average the contiguous voxels in the three directions, we obtain the mean local pore size. Repeating this process for all pore voxels, mean pore size can be calculated and also pore size distributions were obtained (Figure 2). These histograms can be gracefully used to assess the effectiveness of the scaffold manufacture process.

Structure Index. St.I was quantified by the struts' St.Th and SV. This parameter provides a relationship between SV and the mean structure thickness. It is calculated by the following:

$$\mathrm{St.I} = \frac{\mathrm{SV}}{\mathrm{St.Th}} \tag{6}$$

Fractal Analysis. The degree of complexity or disorder of the spongy microarchitecture can be studied using fractal techniques. Our Fractal analysis was based on the calculation of Fractal dimension parameter (D) of each image.[39] It was done by applying a box-counting algorithm that consisted of superposing a grid of a square edge λ on the image and counting the squares containing boundaries (N); this process was repeated with other values of square edge. Different values of the fraction $\ln(N)/\ln(\lambda)$ were obtained determining a straight line which slope m is related to Fractal dimension $D = -m$.

The value of 2D Fractal Dimension in spongy microarchitectures is closely related to structural properties like porosity and connectivity,[37] showing that this parameter can be used to evaluate and characterize porous structures like polymer scaffolds or trabecular bone.

Topological Study. Structural degree of erosion can be quantified by a topological characterization of the voxels in the structure. Therefore, structure voxels must be classified depending on its relative position to develop a topological study. All voxels of the 3D reconstruction were ordered into different classes based on the combination of 2D basic elements (curves and surfaces). Before the classification method was performed, a 3D skeletonization algorithm was applied to obtain a shape reconstruction of the original structure.[40]

Classification was developed as in Refs. 41 and 42, defining nine types of voxels (Surface interior, S; Surface–surface junction, SS; Surface-Edge, SE; Surface-Curve junction, SC; interior Curve, C; Curve-Curve junction, CC; Curve-Edge, CE; Profile, P; and Isolated, I).

Once all topological information was discriminated (all voxels topologically classified), topological parameters SCR (surface-to-curve ratio) and TEI (total erosion index) were obtained by[7,8] the following:

$$\mathrm{SCR} = \frac{S + \mathrm{SE} + \mathrm{SS}}{C + \mathrm{CC} + \mathrm{CE} + P/2} \tag{7}$$

$$\mathrm{TEI} = \frac{C + \mathrm{CC} + \mathrm{CE} + \mathrm{SE} + P}{S + \mathrm{SS}} \tag{8}$$

As it can be inferred in, Ref. 7 SCR represents the ratio between densities of all voxel types related to surfaces and voxel types belonging to curves. In the same way, TEI represents the quotient of dividing all those voxel densities regarding curves (eroded elements) by surface voxel densities.

Finite Element Modeling

Compression stress–strain test was numerically simulated to compare the mechanical properties of the specimen in the initial linear range with those obtained from experimental measurements. Bulk material properties employed in the FE model were experimentally measured by us by stress–strain compression tests at room temperature (Table I).

Finite element analysis was developed with Ansys Package v10.0 (Ansys, Southpointe, PA), using isotropic hexahedron elements (brick elements) with quadratic interpolation functions.

Finite element modeling (FEM) was performed on scaffold meshed samples of 1.5 mm × 1.5 mm × 1 mm approximately. Finite Element models of the corresponding scaffolds have a mean number of 2,186,272 nodes and 1,275,169 elements and were built in MATLAB by direct conversion from voxels from the 3D reconstruction (image data) to brick elements (structural data) using a fast mesher algorithm developed by us. Material properties, node coordinates, and element connectivity were assembled in a ASCII file to be imported directly to Ansys. After the model was imported, constraints were defined to carry out a uniaxial compression test. Null displacement was imposed on nodes from one side of the sample, whereas a negative displacement was specified on nodes from the opposite side to simulate compression. Displacement was set to 10% of the edge length. Once the solution was calculated, reactions on nodes (F_n) from the fixed side were processed to obtain an apparent elastic modulus of the specimen by the following:

$$E = \frac{1}{\varepsilon A}\sum_n F_n \tag{9}$$

As can be observed in Ref. 9, homogenization approximation was supposed in the fraction of the total sum value of the nodal reactions of the fixed size by the area (A) of the corresponding side.[43] Last quotient was then divided by the global deformation of the sample (ε) and finally an apparent Young's module was obtained for the whole structure.

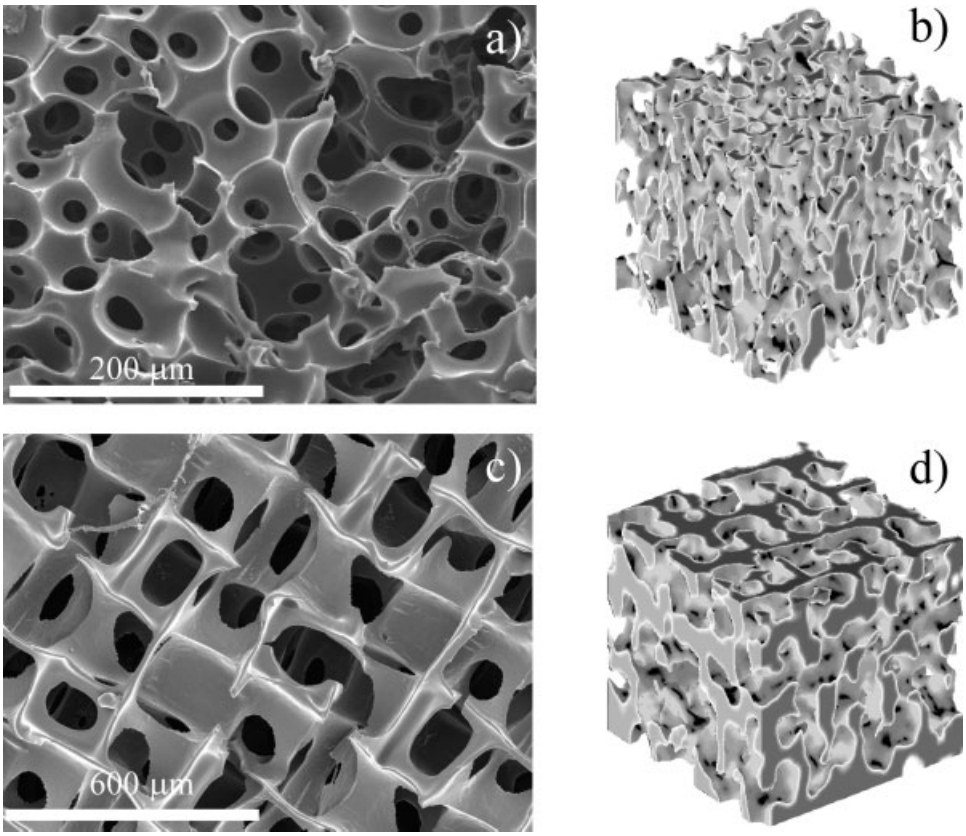

Figure 1. SEM micrographs (a, c) and reconstruction from image analysis (b, d) of the different structures: interconnected spherical pores (a, b) and mesh of orthogonal channels (c, d).

RESULTS

Figure 1 shows the SEM micrographs of the investigated scaffolds and the corresponding 3D reconstruction after the image analysis from the μCT sections. Figure 1(a) shows the 3D spherical interconnected porous network. The porosity of the scaffold might be changed, for a fixed pore size according to the diameter of the porogen sphere employed ($\sim$90 μm), by changing the pressure conditions of the sintered template. The scaffolds employed in this work were fabricated by keeping approximately the same porosity (80%) but changing the hydrophilicity of the system so that qualitatively different mechanical (and physico-chemical properties) properties could be obtained. Figure 1(c) shows the scaffolds with a well-ordered mesh of cylindrical pores. The front view showing the interconnections can be observed.

The corresponding 3D reconstructions of micro-CT data are shown in Figure 1(b,d). Some similarities can be observed between the SEM images and the reconstructed ones after direct observation. The average porosity as obtained from the image analysis and the experimental one are shown in Table I. There is good agreement between the calculated and experimental porosities being the maximum difference below 0.05. Furthermore, the image analysis of the μCT sections allows one to calculate a set of topological parameters which cannot be obtained by other techniques. Figure 2 shows the pore size distributions for the different scaffolds. Pore sizes between 40 and 200 μm are obtained for the interconnected spherical pores [Figure 2(a–c)].The average pore size is around 90–100 μm independent of the chemical composition of the scaffold. Pore size ranges between 40 and 250 μm for the scaffold with a mesh of orthogonal channels. Its distribution is not symmetric with maximum around 100 μm and means around 150 μm [Figure 2(d)].

Figure 3 shows typical experimental compressive stress–strain curve for one of our scaffolds. The curve consists of four phenomenological different zones. At very low strains (lower than 0.03, zone (a)), there is a curved part due to the process of adaptation between the sample, which is not perfectly flat, and the compression plates. Afterwards, the stress–strain relationship is linear up to a strain equal to 0.1 (zone (b)). The experimental moduli of the porous structures were calculated from the slope of initial linear part of the curve, as indicated by the straight dotted line in the graph, zone (b). Subsequently, there is a broad range of strains (approximately between 0.1 and 0.4) that the stress does hardly change from 1 to 2 MPa (zone (c)). Finally, the stress varies quickly on the strain again (it changes from 3 to 5 MPa as strain increases from 0.4 to 0.6).

The elastic modulus depends on the composition of the system for the structures that consists of interconnected spherical pores: as the HEA amount in the system

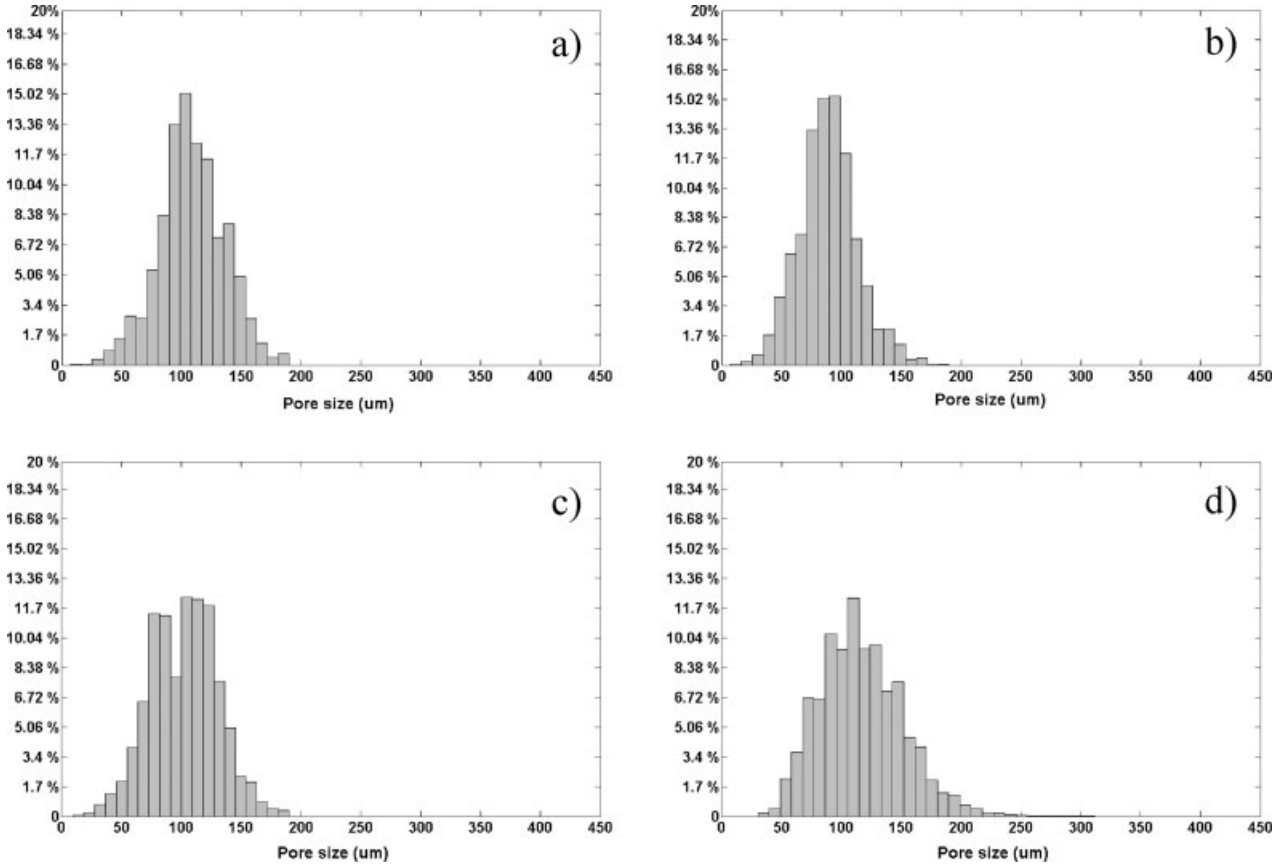

Figure 2. Pore size distributions for the investigated structures. (a–c) Interconnected spherical pores of different compositions (CLMA sample (a), CLMA 50 (b), CLMA30 (c). (d) Mesh of orthogonal channels.

increases, the modulus does. The normalized (relative to the bulk) experimental moduli for the materials are depicted in Figure 4. Table I includes the experimentally measured modulus for scaffolds (E) and bulk materials (E_b), whose ratio gives rise to the normalized moduli. The elastic modulus decreases as porosity increases.

Figure 4 shows the results from the FEM simulations for the different scaffolds. The normalized modulus (relative to the bulk) as a function of the square of porosity follows a straight line (Figure 4). The dependence of the normalized modulus *versus* Structure Thickness (St.Th), Structure Index (St.I), and Fractal Dimension (D) obtained from the μCT image analysis have been plotted in Figure 5(a–c). After applying the topological analysis, values grading the erosion of the scaffolds were obtained (Table I). These parameters (SCR and TEI) allow one to quantify the topology of the scaffolds, which describe how the scaffold is assembled in terms of connectivity and orientation of the 3D architecture. Table I shows these parameters to be independent of the mechanical properties.

Figure 6 shows the distribution of maximum difference between principal stresses at each element for the different architectures investigated in this work: interconnected spherical pores and orthogonal channels.

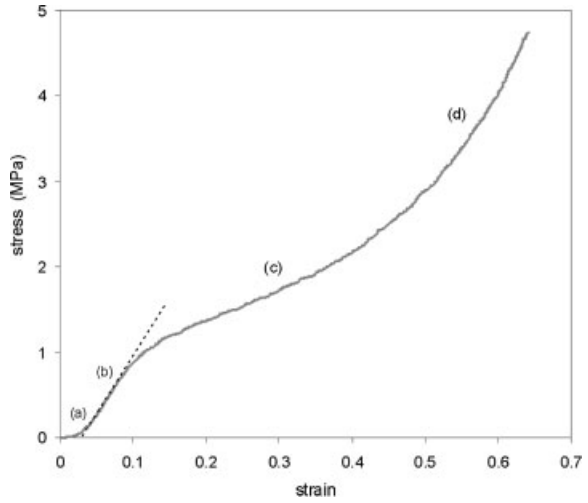

Figure 3. Experimental stress–strain curve of a scaffold with interconnected spherical pores. The letters on the curve are related to different mechanical features as explained in the text. Briefly: (a) contact region between the sample and the device; (b) the linear elastic region (the elastic modulus was calculated from the slope of the dotted line); (c) buckling phenomenon leading to the so-called plateau; and (d) final collapse of the structure increasing the compressive modulus.

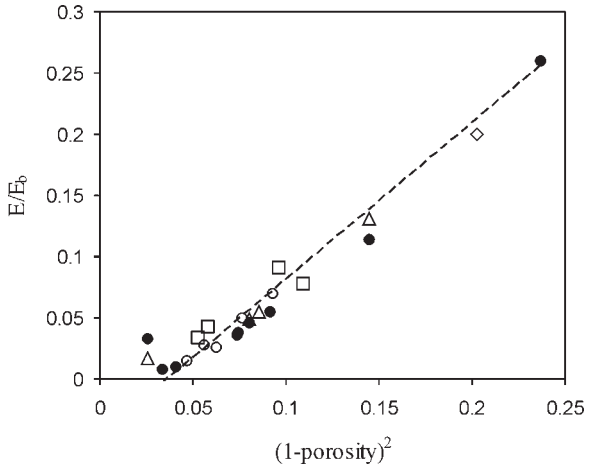

Figure 4. μFEM calculated (●) and experimentally measured normalized (to the bulk E_b) moduli for the different structures: (□) constructs with spherical pores, (◊) construct with orthogonal cylindrical pores, (Δ) construct based on salt particles. Additional points (O) from Ref. 44 have been included so as to reinforce the universality of the relationship between the (reduced) elastic modulus and porosity. The dashed line corresponds to the linear fit with slope $C = 1.28$ [Eq. (10)].

DISCUSSION

The relationship between the architecture of three different polymer scaffolds and their mechanical properties are shown in this work. On the one hand, the network of interconnected spherical pores [Figure 1(a)], the structure based on interconnected pores obtained from salt particles (not shown), and the one which consists of interconnected longitudinal channels along three orthogonal axes [Figure 1(b)].[36] Besides, the materials chemistry and hydrophilicity of the material forming the first structure has been modified in a broad range. In all cases, μCT acquisition achieves a very high-spatial resolution (considering the designed pore sizes) capable of minimizing partial volume effects and ease the process of binarization.[31,32]

Image processing techniques represent a powerful tool to develop a structural and mechanical characterization of the scaffolds and check the achievement of the desired properties at the manufacture stage.[25,28] According to synthesis specifications, pore size and porosity were successfully calculated using 3D techniques, whereas published studies are mainly focused on 2D methods.[34] The total porosity calculated from image analysis is similar to that calculate experimentally (difference lower than 0.05 in any case, Table I). Furthermore, image analysis allows one to calculate, in a nondestructive manner, the pore size distribution [Figure 2(a–d)]. Symmetric pore distributions are obtained for the scaffolds which consist of spherical pores. The maximum is approximately located at 90 μm, which agrees with the nominal diameter of the PMMA porogen employed during the fabrication process. The shape of the distribution is mostly unaffected by the chemical composition of the scaffold, that is, the architecture of the scaffold is mainly determined during the sinterization process of the PMMA template and it does not change due to the polymerization of different chemical components. This could happen since the PMMA porogen is better swollen by the monomer solution richer in CLMA leading to pore collapse after the fabrication process.[45] However, the results of the image analysis [Figure 2(a–d)] disregards this possibility.

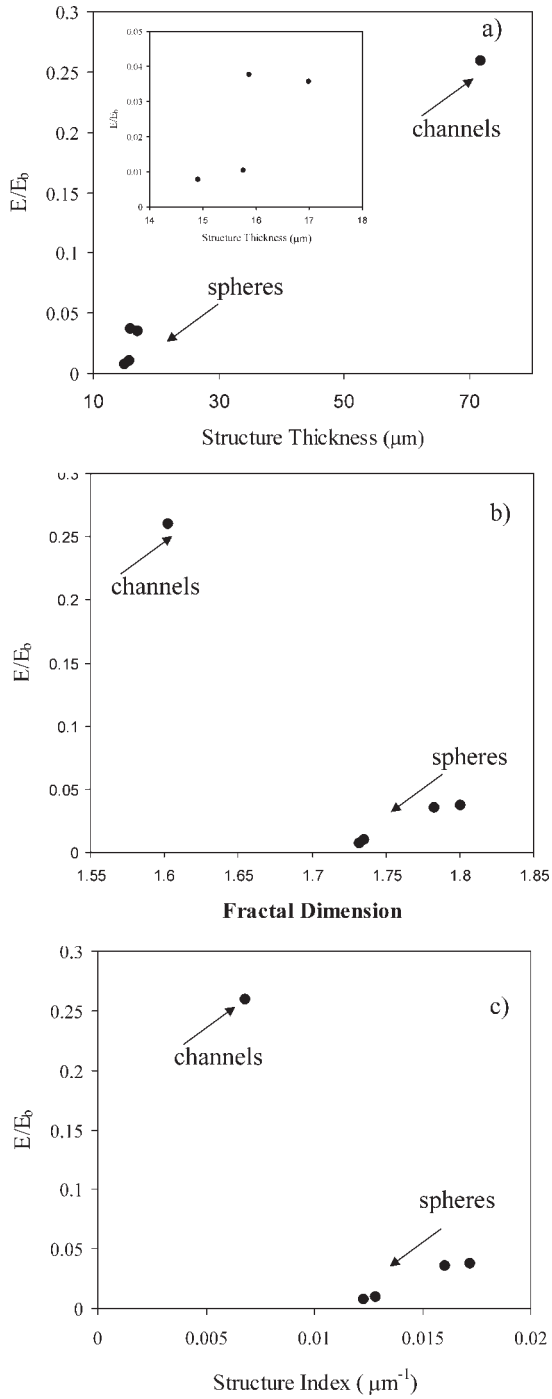

Figure 5. Normalized elastic modulus *versus* structure thickness (a), fractal dimension (b), and structure index (c) for the different structures. Inset in Figure 5(a) magnifies data around 15 μm.

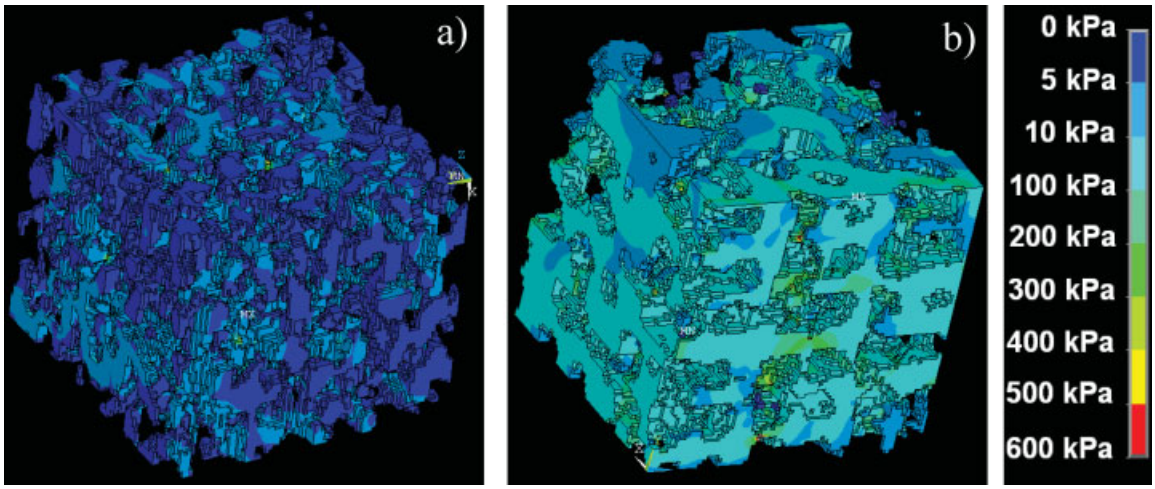

Figure 6. Maximum difference between principal stresses at each element. (a) Scaffold with interconnected spherical pores. (b) Scaffold with orthogonal channels. Color scale goes from 5 kPa (dark blue) to 600 kPa (red). [Color figure can be viewed in the online issue, which is available at www.interscience.wiley.com.]

The pore size distribution of the second structure [interconnected channels, Figure 2(d)] is less symmetric (with a long tail toward the high pore sizes), with maximum around 100 μm and mean around 150 μm, in excellent agreement with the nominal tread diameter of the commercial textile fabric employed as a porogen.[36]

Comparing topology results for the different architectures, the scaffold based on cross-linked channels presents a higher number of structure surfaces (lower erosion) than the CLMA sample, which has large pore sizes whose structure topology is mainly based on beams or rods. However, as the pore size diminishes, erosion index tends to be similar for both architectures due to the increment of surface topology.

The material which constitutes the scaffolds walls is a rubber at room temperature in any case (the glass transition temperatures have been included in Table I). Figure 3 shows a characteristic stress–strain curve for one of the scaffolds which constitute open-cell foams. After an initial region of contact between sample and compression plates (a), a linear elastic zone appears where the compressive modulus was calculated (b). The linear elastic region is controlled by cell wall bending of the scaffold walls. Afterwards, a loss of linearity is observed, the so-called plateau (c), due to the buckling phenomenon (this region is difficult to distinguish for low stiffness specimens). Buckling is characteristic of elastomeric foams (this is our case, see the glass transition temperature in Table I) and differs from the formation of plastic hinges in metals and brittle crushing in ceramics. Finally, the densification of the material occurs when pores become together and collapse the structure, increasing the compressive modulus as a result of the final region of increasing stress (d). The mechanism associated to each region of the curve has been described for other cellular solids of similar structures.[2,44,46] The reduced modulus (relative to the bulk) has been included in Figure 4.

μFEM was performed on the different structures so as to get a better understanding of the mechanical properties on the topological characteristics of the scaffold. The identification of one node to each voxel gives rise to high-computational requirements, especially when the number of nodes tends to be greater than 10^6 due to the large stiffness matrix to be assembled. The elastic modulus of the porous structure (E) was efficiently estimated by the homogenization theory approximation, based on linear elastic behavior and small deformations theory.[47] Figure 4 shows the dependence of the reduced modulus (to the bulk) as a function of the square of porosity. Both experimental and μFEM simulations from a different family of scaffolds (those based on salt particles) as well as experimental points from Ref. 44 have been added so as to strength the discussion. Both the experimental measurements and the μFEM results are well correlated with the proposed parabolic dependence for the compressive modulus on porosity[46]

$$\frac{E}{E_b} = C\left(\frac{\rho}{\rho_b}\right)^2 \tag{10}$$

where ρ and ρ_b are the apparent density of the scaffold and bulk density of the constituting material, respectively. The relative density is related to porosity P,

$$\frac{\rho}{\rho_b} = 1 - P \tag{11}$$

The prediction of Eq. (10) (Figure 4, dotted line), with $C = 1.28$ ($R^2 = 0.99$), accounts for the experimental and the predicted FEM model moduli with several porosities, different chemical composition, and, more importantly, with very different architecture (interconnected spheres and

ordered cylindrical orthogonal pores). This result suggests the existence of a universal relationship (in the elastic regime) between the modulus and porosity. This was already suggested by us in a previous work in which interconnected spherical pores of different sizes and interconnected throats were investigated.[44] It is convenient to note that linear dependence of the reduced modulus on porosity (Figure 4) does not extrapolate to zero when porosity tends to one. This suggests the existence of a minimum amount of material to get the adequate connection so that the dimensional stability is enough to measure the modulus. The relationship shown in Eq. (10) is well-known for open cellular solids. Gibson and Ashby's book[46] shows experimental results for some 20 different studies and the data correlate with the analytical solution with $C = 1$. The equation is deduced in the book following dimensional arguments based on simple expressions from strength of materials. Our results support this expression in two ways as follows: (i) by comparing it with mechanical measurements performed on synthetic scaffolds and finite element method (i.e., linear elasticity) and (ii) by showing, with very different architectures, that total porosity is the only one parameter which influences the elastic properties of the scaffold. Moreover, even if Eq. (10) can be considered to be completely general in the elastic regime, valid for any kind of material, there is still the constant C that is said to depend (see Gibson and Ashby's book, Ref. 46) on the pore "shape." We show that it is not the case.

The normal stress distribution is somehow different for the different architectures. Figure 6(a) shows that the interconnected spherical pores results in a homogeneous stress distribution and pores do not act as stress concentrators as it would happen if only one of spherical pore were surrounded by the scaffolding material. On the other hand, the structure which consists of orthogonal channels shows some stress concentration nearby the channels [Figure 6(b)], which can be accounted for the anisotropy of the spatial architecture as well as the lower porosity compared with that of spherical pores.[35]

The combined use of image analysis (from μCT) and μFEM allows one to investigate the correlation of the elastic modulus on other topological parameters. The elastic modulus is not well correlated with the structure thickness in a universal way [Figure 5(a)], not even if only the scaffolds based on the spherical pores are considered [see the inset in Figure 5(a)]. The absence of correlation between the compressive modulus and structure thickness was also found in oriented scaffolds.[22] However, structure thickness range in Figure 5(a) is not well-distributed (values ranging between 15 and 20 μm correspond to the spherical pores and the value of 70 μm is related to the structure with interconnected channels) and more data are needed to confirm this lack of correlation. On the other hand, the modulus seems to increase as the fractal dimension of the structure does, as long as the same 3D architecture is considered [Figure 5(b)]. However, when qualitatively different structures are considered, the correlation vanishes (Figure 5). Something similar happens in the modulus dependence on the structure index [Figure 5(c)]. It is noteworthy that even if the architecture of the two porous structures are very different (as it is reflected from the values of the topological parameters in Figure 5) they fall on the same line of modulus *versus* $(1 - P)^2$. This result suggests the lack of influence of scaffold architecture in open foam cells and remarks the validity of total porosity, through Eq. (10), as the unique universal relation in the elastic linear regime.

The good correlation between the μFEM simulations and the experimental results shows the viability of the technique as a feasible tool for scaffold design and advance analysis before physical experiments are performed on real-fabricated scaffolds.

CONCLUSIONS

We have made use of μCT to obtained detailed information of the porous architecture of qualitatively different porous scaffolds for tissue engineering applications. The total porosity, as calculated from the image analysis, is in good agreement with the experimental one. Besides image analysis allows one to calculate the pore size distribution that is, in any case, well-correlated with the dimensions of the porogens employed during the preparations of the scaffolds.

The algorithm employed for the image analysis process allows one to perform detailed numerical simulations of the mechanical properties in the micro scales, so-called μFEM. Our results confirm the hypothesis that the (elastic) mechanical modulus of porous scaffolds depends on the total porosity of the system and not on either the pore shape, or any other topological parameter calculated on the 3D structure (structure thickness, fractal dimension, structure index). Overall, after analyzing three qualitatively different scaffolds architectures prepared with very different techniques, based on different materials chemistry our results support the existence of a universal relationship between total porosity and elastic modulus.

The authors like to thank Victor Alastrué and José Antonio Sanz (Grupo de Estructuras Mecánicas y Materiales GEMM Zaragoza, Spain) for their fruitful comments and suggestions. SEM was performed under the technical guide of the Microscopy Service at the Universitat Politècnica de València. D.M. acknowledges the financial support from the Programa de Apoyo a la Investigación y Desarrollo of the Universitat Politècnica de València. J.L.E.I. acknowledges Generalitat Valenciana for the support through the predoctoral grant. M.S.S. acknowledges the financial support from the Spanish Ministry of Science (including the FEDER financial support).

REFERENCES

1. Langer R, Vacanti JP. Tissue engineering. Science 1993;260: 920–926.

2. Hutmacher DW. Scaffolds in tissue engineering bone and cartilage. Biomaterials 2000;21:2529–2543.
3. Freed LE, Hollander AP, Martin I, Barry LR, Vunjak-Novakovic G. Chondrogenesis in a cell-polymer-bioreactor system. Exp Cell Res 1998;240:58–65.
4. Yang S, Leong K-F, Du Z, Chua C-K. The design of scaffolds for use in tissue engineering. I. Traditional factors. Tissue Eng 2001;7:679–689.
5. Gao CY, Wang DY, Shen JC. Fabrication of porous collagen/chitosan scaffolds with controlling microstructure for dermal equivalent. Polym Adv Technol 2003;14:373–379.
6. Horbett TA, Schway MB, Ratner BD. Hydrophilic-hydrophobic copolymers as cell substrates-effect on 3T3 cell-growth rates. J Colloid Interface Sci 1985;104:28–39.
7. Zhang R, Ma PX. Poly(α-hydroxyl acids)/hydroxyapatite porous composites for bone-tissue engineering. I. Preparation and morphology. J Biomed Mater Res 1999;44:446–455.
8. Gibson LJ. Biomechanics of cellular solids. J Biomech 2005; 38:377–399.
9. Roberts AP, Garbozi EJ. Elastic moduli of model random three-dimensional closed-cell cellular solids. Acta Mater 2001;49:189–197.
10. Whang K, Thomas CH, Healy KE. A novel method to fabricate bioabsorbable scaffolds. Polymer 1995;36:837–842.
11. Harris LD, Kim BS, Mooney DJ. Open pore biodegradable matrices formed with gas foaming. J Biomed Mater Res 1998;42:396–402.
12. Thomson RC, Wake MC, Yaszemski M, Mikos AG. Biodegradable polymer scaffolds to regenerate organs. Adv Polym Sci 1995;122:247–274.
13. Mikos AG, Sarakinos G, Leite SM, Vacanti JP, Langer R. Laminated 3-dimensional biodegradable foams for use in tissue engineering. Biomaterials 1993;14:323–330.
14. Zhou QL, Gong YH, Gao CY. Microstructure and mechanical properties of poly(L-lactide) scaffolds fabricated by gelatin particle leaching method. J Appl Polym Sci 2005;98:1373–1379.
15. Moroni L, de Wijn JR, Blitterswijk CA. 3D fiber-deposited scaffolds for tissue engineering: Influence of pores geometry and architecture on dynamic mechanical properties. Biomaterials 2006;27:974–985.
16. Hollister SJ. Porous scaffold design for tissue engineering. Nat Mater 2005;4:518–524.
17. Engelmayr GC, Papworth GP, Watkins SC, Mayer JE, Sacks MS. Guidance of engineered tissue collagen orientation by large-scale scaffold microstructures. J Biomech 2006;39: 1819–1831.
18. Ho ST, Hutmacher DW. A comparison of micro CT with other techniques used in the characterization of scaffolds. Biomaterials 2006;27:1362–1376.
19. Feldkamp LA, Goldstain SA, Parfitt AM, Jesion G, Kleerekope M. The direct examination of three-dimensional bone architecture in vitro by computed tomography. J Bone Miner Res 1989;4:3–11.
20. Kapadia RG, Stroup GB, Badger AM, Koller B, Levin JM, Coatney RW, Dodds RA, Liang X, Lark MW, Gowen M. Applications of micro-CT and MR microscopy to study preclinical models of osteoporosis and osteoarthritis. Technol Health Care 1998;6:361–372.
21. Yamashita T, Nabeshima Y, Noda M. High-resolution microcomputed tomography analices of the abnormal trabecular bone structures in Klotho gene mutant mice. J Endocrinol 2000;164:239–245.
22. Lin ASP, Barrows TH, Cartmell SH, Guldberg RE. Microarchitecture and mechanical characterization of oriented porous polymer scaffolds. Biomaterials 2003;24:481–489.
23. Wang F, Shor L, Darling A, Khalil S, Sun W, Guceri S, Lau A. Precision extruding deposition and characterization of cellular poly e-caprolactone tissue scaffolds. Rapid Prototyping J 2004;25:1683–1696.
24. Darling AL, Sun W. 3D microtopographic characterization of precision extruded poly-e-caprolactone scaffolds. J Biomed Mater Res B Appl Biomater 2004;15:311.
25. Cancedda R, Cedola A, Giuliani A, Komlev V, Lagomarsino S, Mastrogiacomo M, Peyrin F, Rustichelli F. Bulk and interface investigations of scaffolds and tissue-engineered bones by X-ray microtomography and X-ray microdiffraction. Biomaterials 2007;28:2505–2524.
26. Jones AC, Milthorpe B, Averdunk H, Limaye A, Senden TJ, Sakellariou A, Sheppard AP, Sok RM, Knackstedt MA, Brandwood A, Rohner D, Hutmacher DW. Analysis of 3D bone ingrowth into polymer scaffolds via micro-computed tomography imaging. Biomaterials 2004;25:4947–4954.
27. Gauthier O, Müller R, von Stechow D, Lamy B, Weiss P, Bouler J-M, Aguado E, Daculsi G. In vivo bone regeneration with injectable calcium phosphate biomaterial: A three-dimensional micro-computed tomographic, biomechanical and SEM study. Biomaterials 2005;26:5444–5453.
28. Otsuki B, Takemoto M, Fujibayashi S, Neo M, Kokubo T, Nakamura T. Pore throat size and connectivity determine bone and tissue ingrowth into porous implants: Three-dimensional micro-CT based structural analyses of porous bioactive titanium implants. Biomaterials 2006;27:5892–5900.
29. Jones AC, Arns CH, Sheppard AP, Hutmacher DW, Milthorpe BK, Knackstedt MA. Assessment of bone ingrowth into porous biomaterials using MICRO-CT. Biomaterials 2007;28: 2591–2504.
30. van Lenthe GH, Hagenmüller H, Bohner M, Hollister SJ, Meinel L, Müller R. Nondestructive micro-computed tomography for biological imaging and quantification of scaffold-bone interaction in vivo. Biomaterials 2007;28:2749–2490.
31. Adachi T, Tsubota K, Tomita Y, Hollister SJ. Trabecular surface remodeling simulation for cancellous bone using microstructural voxel finite element models. J Biomech Eng 2001; 123:403–409.
32. Nagaraja S, Couse TL, Guldberg RE. Trabecular bone microdamage and microstructural stresses under uniaxial compression. J Biomech 2005;38:707–716.
33. Jaecques SVN, Van Oosterwyck H, Muraru L, Van Cleynenbreugel T, De Smet E, Wevers M, Naert I, Vander Sloten J. Individualized, micro CT-based finite element modeling as a tool for biomechanical analysis related to tissue engineering of bone. Biomaterials 2004;25:1683–1696.
34. Lacroix D, Chateau A, Ginebra MP, Planell JA. Micro-finite element models of bone-tissue engineering scaffolds. Biomaterials 2006;27:5326–5334.
35. Escobar Ivirico JL, Costa Martínez E, Salmerón Sánchez M, Muñoz Criado I, Gómez Ribelles JL, Monleón Pradas M. Methacrylate-endcapped caprolactone networks hydrophilized by copolymerization with 2-hydroxyethyl acrylate. J Biomed Mater Res B Appl Biomater 2007;83B:266–275.
36. Rodríguez Hernández JC, Serrano Aroca A, Gómez Ribelles JL, Monleón Pradas M. Three-dimensional nanocomposite scaffolds with ordered cylindrical orthogonal pores. J Biomed Mater Res B Appl Biomater 2008;84:541–549.
37. Jianzhuang L, Wenqing L, Yupeng T. Automatic thresholding of gray-level pictures using two-dimension Otsu method. International Conference on Circuits and Systems, China: Conference Proceedings; 1991. Vol. 1, pp 325–327.
38. Saha PK, Wehrli FW. Measurement of trabecular bone thickness in the limited resolution regime of in vivo MRI by fuzzy distance transform. IEEE Trans Med Imaging 2004;23:53–62.
39. Pothuaud L, Benhamou CL, Porion P, Lespessailles E, Harba R, Levitz P. Fractal dimension of trabecular bone projection texture is related to three-dimensional microarchitecture. J Bone Miner Res 2000;15:691–699.

40. Saha PK, Chaudhuri BB, Majumder DD. A new shape preserving parallel thinning algorithm for 3D digital images. Pattern Recognit 1997;30:1939–1955.
41. Gomberg BR, Saha PK, Song HK, Hwang SN, Wehrli FW. Topological analysis of trabecular bone MR images. IEEE Trans Med Imaging 2000;19:166–174.
42. Saha PK, Gomberg RB, Wehrli FW. Three-dimensional digital topological characterization of cancellous bone architecture. Int J Imaging Syst Technol 2000;11:81–90.
43. Hollister SJ, Kikuchi N. A comparison of homogenization theory and standard mechanics analyses for periodic porous composites. Comput Mech 1992;10:73–95.
44. Brígido Diego R, Más Estellés J, Sanz JA, García-Aznar JM, Salmerón Sánchez M. Polymer scaffolds with interconnected spherical pores and controlled architecture for tissue engineering: Fabrication, mechanical properties and finite element modelling. J Biomed Mater Res B Appl Biomater 2007;81B: 448–455.
45. Brígido Diego R, Gómez Ribelles JL, Salmerón Sánchez M. Pore collapse during the fabrication process of rubber-like polymer scaffolds. J Appl Polym Sci 2007;104:1475–1481.
46. Gibson LJ, Ashby M. The mechanics of foam: Basic results. In: Clarke DR, Suresh S, Ward IM, editors. Cellular Solids: Structure and Properties. Cambridge: Cambridge University Press; 2001. pp 175–234.
47. Kouznetsova VG. Computational homogenization for the multiscale analysis of multi-phase materials, PhD thesis. The Netherlands: Technical University of Eindhoven; 2002.